

Statistical spatial analysis for cryo-electron tomography

Antonio Martinez-Sanchez^{1,2,3,4,5*}, Wolfgang Baumeister⁵ and Vladan Lučić^{5,*}

July 15, 2021

¹Department of Computer Sciences, Faculty of Sciences - Campus Llamaquique, University of Oviedo, 33007 Oviedo, Spain

²Health Research Institute of Asturias (ISPA), Avenida Hospital Universitario s/n, 33011 Oviedo, Spain

³Institute of Neuropathology, University Medical Center Göttingen, Göttingen, Germany

⁴Cluster of Excellence "Multiscale Bioimaging: from Molecular Machines to Networks of Excitable Cells" (MBExC), University of Göttingen, Göttingen, Germany

⁵Department of Molecular Structural Biology, Max Planck Institute for Biochemistry, Am Klopferspitz 18, 82152 Martinsried, Germany

*E-mail: martinezsantonio@uniovi.es, vladan@biochem.mpg.de

Abstract

Cryo-electron tomography (cryo-ET) is uniquely suited to precisely localize macromolecular complexes *in situ*, that is in a close-to-native state within their cellular compartments, in three-dimensions at high resolution. Point pattern analysis (PPA) allows quantitative characterization of the spatial organization of particles. However, current implementations of PPA functions are not suitable for applications to cryo-ET data because they do not consider the real, typically irregular 3D shape of cellular compartments and molecular complexes. Here, we designed and implemented first and the second-order, uni- and bivariate PPA functions in a Python package for statistical spatial analysis of particles located in three dimensional regions of arbitrary shape, such as those encountered in cellular cryo-ET imaging (PyOrg).

To validate the implemented functions, we applied them to specially designed synthetic datasets. This allowed us to find the algorithmic solutions that provide the best accuracy and computational performance, and to evaluate the precision of the implemented functions. Applications to experimental data showed that despite the higher computational demand, the use of the second-order functions is advantageous to the first-order ones, because they allow characterization of the particle organization and statistical inference over a range of distance scales, as well as the comparative analysis between experimental groups comprising multiple tomograms.

Altogether, PyOrg is a versatile, precise, and efficient open-source software for reliable quantitative characterization of macromolecular organization within cellular compartments imaged *in situ* by cryo-ET, as well as to other 3D imaging systems where real-size particles are located within regions possessing complex geometry.

1 Introduction

The last decades of research in cell biology have revealed that cellular processes are performed by groups of interacting macromolecules in a crowded environment. This is in contrast to earlier models where macromolecules were considered to exist as isolated objects floating randomly in the cytoplasm. Therefore the analysis of their organization within their native cellular compartments can provide quantitative information that can be used to describe the mechanisms underlying macromolecular interactions. This information has paramount importance to gain a deeper understanding of various cellular interactions [1, 2].

Cryo-Electron Tomography (cryo-ET) is a unique imaging technique capable of producing 3D views of large portions of cells at a resolution that is sufficiently high to localize and identify macromolecular complexes [3].

In cryo-ET, biological samples are vitrified to preserve their natural molecular organization and are imaged by electron microscopy in the fully-hydrated vitrified state, thus enabling the study of cells in a close-to-native state at high resolution [4, 5].

Point patterns analysis (PPA) is a branch of statistics devoted to describing quantitatively point patterns in space. PPA has been used extensively in experimental fields such as ecology [6], social sciences [7, 8], and more recently in biology [9, 10]. Among PPA methods, first-order functions describe clustering of points and typically determine a characteristic distance scale, whereas second-order functions determine spatial correlations between points at a range of distances. Ripley’s functions K (or its linearization, L) and O [6] are the most used tools for second-order PPA. They have been used for analyzing experimental biological data obtained from light and electron microscopy [10, 11, 12]. Current implementations of the PPA methods were either developed for 2D spaces [13], or their application in 3D is limited to sphere-shaped structures within cubic volumes [11, 14]. However, these approaches have two limitations, rendering their application impractical for cellular cryo-ET data: (i) cellular compartments have complex geometry so, there are no analytical solutions for border compensation, unlike for the most simple geometries [15, 14], and (ii) proteins have specific shapes that can not be properly represented by points or spheres. Recently Voronoi tessellation has been used to describe the particle organization in super-resolution optical microscopy [16], but contrarily to Ripley’s functions it does not allow comparison between datasets having different density of points.

The authors have already applied PPA functions to successfully solve some long-standing biological questions. Firstly, in [2], we applied a modification of Ripley’s function O to prove that Rubisco complex has a liquid-like organization within the pyrenoid organelle, thus discarding crystalline models proposed previously. This finding was also remarkable as cryo-ET data was used to successfully analyze a phase-separated compartment *in situ* at nanometric resolution for the first time. We also showed that the Arp2/3 complex within actin waves modifies its clustered organization depending on the wave-phase [17]. Recently, we demonstrated that Ripley’s functions can be used to characterize nano-domains formed by synaptic membrane-bound complexes [18].

Here we present an implementation of the first and second order PPA functions where both particles and cellular compartments can be of arbitrary shape. Consequently, these functions are applicable to cryo-ET images of cellular samples, that is they are suitable for the spatial distribution analysis of individual proteins or macromolecular complexes localized in any kind of cellular compartment (cytoplasm, organelle lumen, membrane, etc). These numerical calculations are required to precisely calculate the computationally intensive second order PPA functions. We also present a parallel implementation suitable for processing cryo-ET datasets that takes advantage of modern multiprocessor architectures [19]. In addition to univariate PPA functions, we also implemented the bivariate versions of PPA functions, which enable the colocalization analysis between different proteins and macromolecules.

We present several applications to synthetic datasets in order to compare different numerical methods and find the most appropriate ones. Finally, we also applied the methods we implemented on real Cryo-ET datasets to validate their real-case usability and to justify the necessity for an accurate implementation of second-order PPA function.

2 Approach

In this section, we show the implementation details relevant for the first and second order PPA functions, for univariate and bivariate cases.

2.1 Design

2.1.1 Monivariate first-order analysis

Nearest neighbor function G , spatial contact distribution function F , and their combination J belong to the first order PPA functions. Location of proteins or macromolecular complexes of interest (particles) in a tomogram (3D image) is defined by their spatial coordinates $\mathbf{X} = \{\mathbf{x}_i \in \mathcal{V} \forall i = (1, \dots, n)\}$, where n is the number of

particles and $\mathcal{V} \in \mathbb{R}^d$ is the Volume of Interest (VOI), that is a subspace of the tomogram where the particles are located. A VOI typically represents an organelle or a distinct cellular compartment.

Function G is defined as:

$$G(r) = \int_0^r p_G(r) dr \quad (1)$$

where $p_G(r)$ is the probability distribution function of nearest neighbor distances r of all particles in \mathbf{X} .

Function F is similarly defined, except that it requires $p_F(r)$, the probability distribution function of nearest neighbor distances among points in sets \mathbf{X} and $\mathbf{X}^{\text{CSR}} \in \mathcal{V}$, where \mathbf{X}^{CSR} is a set of coordinates distributed according to the Complete Spatial Randomness (CSR) model in \mathcal{V} [6, 11]:

$$F(r) = \int_0^r p_F(r) dr \quad (2)$$

The calculation of functions G and F are not computationally demanding even though function F requires the generation of set \mathbf{X}^{CSR} . G is better suited to characterize short scale properties of particle clusters, while F characterizes the space devoid of particles and large scale organization of particle clusters. In order to combine their advantages, function J was defined as:

$$J(r) = \frac{1 - G(r)}{1 - F(r)} \quad (3)$$

However, the practical applications of function J are limited because it is not defined for $F(r) = 1$ and numerical problems appear when $F(r) \rightarrow 1$.

2.1.2 Monivariate second-order analysis

Ripley's functions K , L and O are used for second-order analysis. Because cellular compartments (VOIs) typically have an irregular shape and many particles are found close to the compartment borders, it is not possible to determine edge-corrections for Ripley's functions analytically [15, 6]. Therefore, we proceeded to implement Ripley's function where edge-corrections are performed numerically, for each particle separately. Specifically, function L is obtained by the linearization of Ripley's K function [6], which facilitates the interpretation. For a set of particles located at positions \mathbf{x}_i within a 3D VOI of arbitrary shape \mathcal{V} , Ripley's functions K and L are defined as follows:

$$K(r) = \frac{4\pi r^3}{3} \cdot \frac{\sum_{i=0}^n C(\mathbf{x}, \mathcal{S}_L(\mathbf{x}_i, r))}{\lambda \cdot \sum_{i=0}^n V(\mathcal{S}_L(\mathbf{x}_i, r))} \quad L(r) = \sqrt[3]{\frac{3K(r)}{4\pi}} - r \quad (4)$$

$C(\mathbf{x}, \mathcal{S}_L(\mathbf{x}_i, r))$ is the number of particles located in the neighborhood $\mathcal{S}_L(\mathbf{x}_i, r)$ and $V(\mathcal{S}_L(\mathbf{x}_i, r))$ is the volume of this neighborhood. Neighborhood $\mathcal{S}_L(\mathbf{x}_i, r)$ is defined as the edge-corrected neighborhood of the particle located at \mathbf{x}_i , which is obtained by the intersection of the VOI and the spherical neighborhood of the particle at radius r :

$$\mathcal{S}_L(\mathbf{x}_i, r) = \{\forall \mathbf{x} \in \mathcal{V} | d(\mathbf{x}, \mathbf{x}_i) \leq r\} \quad (5)$$

where d is a distance metric (Fig. 1A). In an unbounded space $\mathcal{V} = \mathbb{R}^3$, or for particles located far from boundaries, $\mathcal{S}_L(\mathbf{x}_i, r)$ is simply a sphere centered at \mathbf{x}_i with radius r .

Ripley's function O is defined as:

$$O(r) = \frac{\sum_{i=0}^n C(\mathbf{x}, \mathcal{S}_O(\mathbf{x}_i, r, \Delta r))}{\sum_{i=0}^n V(\mathcal{S}_O(\mathbf{x}_i, r, \Delta r))} \quad (6)$$

Here, $\mathcal{S}_O(\mathbf{x}_i, r, \Delta r)$ is defined as the edge-corrected shell-like neighborhood around the particle located at \mathbf{x}_i , which is obtained by the intersection of the VOI and the spherical shell or radius r and thickness Δr centered at the particle location (Fig. 1B):

$$\mathcal{S}_O(\mathbf{x}_i, r, \Delta r) = \{\forall \mathbf{x} \in \mathcal{V} | r - \Delta r/2 \leq d(\mathbf{x}, \mathbf{x}_i) \leq r + \Delta r/2\} \quad (7)$$

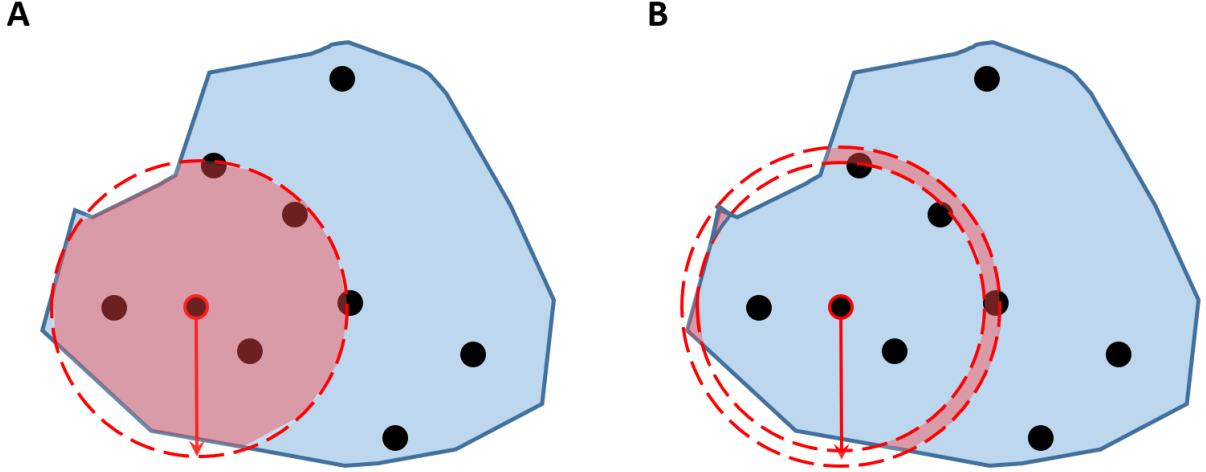


Figure 1: Particle neighborhood and shell for Ripley's functions. (A) Edge corrected particle neighborhood \mathcal{S}_L used for Ripley's L is formed as the intersection of the particle spherical neighborhood (shown as the red circle) and VOI (blue), and is indicated by light red areas. (B) Edge corrected particle shell \mathcal{S}_O used for Ripley's O is formed as the intersection of the particle spherical shell (shown as the red ring) and VOI (blue), and is indicated by light red areas. In both cases particles are represented by black points. Shown in 2D for clarity.

Similarly, in Eq 6, $C(\mathbf{x}, \mathcal{S}_O(\mathbf{x}_i, r, \Delta r))$ is the number of particles located in the shell $\mathcal{S}_O(\mathbf{x}_i, r, \Delta r)$ and $V(\mathcal{S}_O(\mathbf{x}_i, r, \Delta r))$ is the volume of this shell. Therefore, our definitions of $\mathcal{S}_O(\mathbf{x}_i, r)$ and $\mathcal{S}_O(\mathbf{x}_i, r, \Delta r)$ provide edge corrections for functions L and O .

Despite their conceptual similarity, these functions show important differences. Function $O(r)$ can be considered more precise because it depends only on particle pairs having distance close to r , while $K(r)$ and $L(r)$ receive contributions from all scales between 0 and r . However, because $O(r)$ can be understood as a derivative of $K(r)$ it is more affected by noise, especially when the density of particles is low, which limits its usefulness in practice.

2.1.3 Bivariate analysis

The bivariate PPA functions allow investigations of the relationships between two different particle patterns, the reference pattern, $\mathbf{X}^r = \{\mathbf{x}_i^r \in \mathcal{V} | i = (1, \dots, n)\}$, and the evaluation pattern, $\mathbf{X}^e = \{\mathbf{x}_i^e \in \mathcal{V} | i = (1, \dots, n_e)\}$.

The distribution function G for the bivariate analysis is based on the nearest distances among particles between the two different patterns, $p_G^{re}(r)$:

$$G^{re}(r) = \int_0^r p_G^{re}(r) dr \quad (8)$$

where $p_G^{re}(r)$ are distances from all reference particles to their nearest evaluation particles. There is no bivariate counterpart for function F and consequently neither for J .

The bivariate versions of the Ripley's second-order functions analysis show the co-localization of the evaluation particles in respect to the reference particles. These functions are very similar to their monovariate counterparts (Eqs. 4 and 6):

$$K^{re}(r) = \frac{4\pi r^3}{3} \cdot \frac{\sum_{i=0}^n C^e(\mathbf{x}^e, \mathcal{S}_L(\mathbf{x}_i^r, r))}{\lambda^e \cdot \sum_{i=0}^n V(\mathcal{S}_L(\mathbf{x}_i^r, r))} \quad L^{re}(r) = \sqrt[3]{\frac{K^{re}(r)}{4\pi}} - r \quad (9)$$

$$O^{re}(r) = \frac{\sum_{i=0}^n C^e(\mathbf{x}^e, \mathcal{S}_O(\mathbf{x}_i^r, r, \Delta r))}{\sum_{i=0}^n V(\mathcal{S}_O(\mathbf{x}_i^r, r, \Delta r))} \quad (10)$$

except that C^e is the number of evaluation particles \mathbf{X}^e within the edge corrected neighborhood or the shell of reference particles \mathbf{X}^r .

2.1.4 Null-models and statistical inference

In order to determine the statistical significance of particle distribution analysis obtained by the first and second order PPA functions, statistical hypothesis testing methods are used to compare the experimental with the null-model results. Consequently, when generating proper null-models for cryo-ET data, the shape of the particles and cellular compartments has to be considered.

The CSR model was previously defined for point particles located in arbitrary regions [6]. Here we use the Complete Spatial Randomness with Volume exclusion model (CSRv) in 3D, which is an extension of CSR that takes into consideration the 3D shape of particles by imposing volume exclusion to avoid particle overlap. Statistical comparison of experimental results with CSRv null-model allows discarding the random particle distribution hypothesis (the null hypothesis), in which case it can be concluded that the particle organization is controlled by a structural process. Furthermore, this comparison can show whether the experimental distribution is more clustered or more uniformly distributed than CSRv and determine length scale(s) at which the differences are found. A more detailed analysis may require a null-model specifically designed for the actual experimental question [2].

To assess the statistical significance of the results obtained by the first order PPA functions G and F , the Kolmogorov-Smirnov (K-S) test is used. It requires that the variable studied is continuous, and it is applied to the PPA functions represented as the cumulative frequency distribution functions [11] to determine $D_{n,m}$ in the following way:

$$D_{n,m} = \sup_{r_D} |\tilde{G}_n(r) - G_m(r)| \quad (11)$$

$\tilde{G}_n(r)$ is G or F function, obtained from experimental data comprising n particles and $G_m(r)$ the CSRv null-model function, obtained by simulating m synthetic instances of the null-model with the same number of particles and the same VOI as the experimental dataset. The null hypothesis stating that experimental and the simulated distributions are identical can be rejected with the probability $1 - \alpha$ if [20]:

$$D_{n,m} > \sqrt{-\left(\frac{m+1}{2nm}\right) \ln\left(\frac{\alpha}{2}\right)} \quad (12)$$

The K-S test determines a single significance value of a given first order PPA function, by taking into account the entire range of distances that forms its domain. When testing function G , the positive sign of $\tilde{G}_n(r_D) - G_m(r_D)$ specifies that the experimental particles are clustered and the negative sign signifies that they are uniformly distributed. The interpretation is the opposite when testing function F .

For the second order PPA functions, the null hypothesis can be tested by ranking PPA results obtained for multiple null-model simulations and constructing an interval of confidence (IC) as a function of distance r :

$$IC(r) = [IC(r)^-, IC(r)^+] = [L_\alpha(r), L_{1-\alpha}(r)] \quad (13)$$

where $L_\alpha(r)$ is the value of the second order PPA function under consideration that has the rank of $\alpha \cdot 100\%$. If an experimental PPA function falls outside of the interval $IC(r)$ at the distance r , we can reject the null hypothesis with a confidence $1 - \alpha$. Additionally, if the experimental estimator is greater (smaller) than $IC(r)^+$, we can conclude that the pattern is more clustered (more uniformly distributed) than the null-model.

2.2 Methods

2.2.1 Computation of the second-order PPA functions

Efficient implementations of many linear algebra operations that are required to compute the PPA functions introduced above are already available in libraries written in different programming languages. Here we present implementations of the operations that are currently not available in the standard libraries.

The central part of the second-order function computations concerns the determination of the number of particles $C(\cdot)$ and the volume $V(\cdot)$ of local edge corrected neighborhoods \mathcal{S}_L and \mathcal{S}_O . Because the neighborhoods are defined in a VOI of arbitrary geometry \mathcal{V} , these computations cannot rely on closed formulas but require numerical approximations. Therefore, they require computations of kernels for the number of particles and volume for neighborhoods of different radii, for each particle \mathbf{x}_i separately: $C(\mathbf{x}, \mathcal{S}_L(\mathbf{x}_i, r))$, $C(\mathbf{x}, \mathcal{S}_O(\mathbf{x}_i, r, \Delta r))$, $V(\mathcal{S}_L(\mathbf{x}_i, r))$ and $V(\mathcal{S}_O(\mathbf{x}_i, r, \Delta r))$. As a consequence, second-order analysis is computationally much more demanding than first-order analysis. We note that the global particle density can be computed by $\lambda = n/V(\mathcal{V})$.

2.2.2 Counting the number of particles in a region of arbitrary shape

It is critical to choose the most efficient way of evaluating whether a point belongs to a VOI ($\mathbf{x} \in \mathcal{V}$) because this condition is evaluated intensively during the computation of second-order functions. It is required both for the computations involving real data and the randomly generated data used for null-models. Here we consider two approaches that use different ways to represent VOI.

In the surface approach, VOI is represented as a closed surface defined by a triangle mesh. To evaluate the condition $\mathbf{x}_i \in \mathcal{V}$, where \mathbf{x}_i is the particle center, we used the ray-firing method consisting of the following steps: (1) Randomly oriented rays originating at the evaluation point are generated. (2) For each ray, the number of intersections with the bounding surface is counted. (3) If the number of rays having an odd number of intersections is larger than the number of rays having an even number of intersections, the point is considered to belong to the VOI (Fig. 2A).

In the second approach, a VOI is represented by *true* voxels in a dense 3D Boolean array (termed 3D array representation). A point belongs to a VOI simply if it belongs to the set of *true* voxels (Fig. 2B).

It is clear that the surface approach uses less memory than the 3D array approach, even though the array is binary. However, checking the condition $\mathbf{x} \in \mathcal{V}$ for the 3D arrays approach has the complexity $O(1)$, while in the surface approach the complexity is $O(N_{rays})$, where N_{rays} is the number of rays used by the iterative ray-firing method [21]. Our results showed that for both approaches the running time per particle decreased with the number of particles (Fig. S1). This is likely a consequence of the hierarchical cache architecture of current processors. Importantly, for up to 1000 particles, the running time was smaller for the 3D array approach. Only for more than 1000 particles did the running time of the surface approach become comparable to that of the 3D array approach. In addition, the running times were similar for the cases when particles were randomly distributed in a sphere or on a spherical shell.

2.2.3 Estimating the volume of particle neighborhoods

To calculate the volume of an edge corrected neighborhood $V(\mathcal{S})$, we propose two different algorithms. These parallel the approaches to determine whether a point belongs to a region introduced in the previous section.

Monte Carlo surface algorithm (MCS) requires the surface VOI representation. The volume of an edge-corrected neighborhood is calculated by randomly generating points within a spherical neighborhood, using the surface approach to determine whether these points belong to VOI and counting the number of points inside the VOI (Alg. S1, Fig. 3A).

The second, the 3D array algorithm, requires the 3D array VOI representation. The volume of an edge-corrected neighborhood is determined by counting the number of voxels that belong to both the spherical neighborhood and the VOI using the array approach (Alg. S4, Fig. 3B). The 3D array used here has to be large enough to hold the entire neighborhood \mathcal{S} for the largest neighbor radius r . To speed up the computations, the distance between each particle and all other voxels is pre-computed, so that a single distance calculation for a particle can be used for all neighborhoods of that particle.

To evaluate the precision of the neighborhood volume estimation by MCS and 3D array algorithms, we applied them to particles located at the distance of 5 nm to the boundary of a rectangular VOI, and also calculated the edge corrected neighborhood volumes analytically. The volume estimation error E is defined as:

$$E[\%] = \frac{\hat{V} - V}{V} \cdot 100 \quad (14)$$

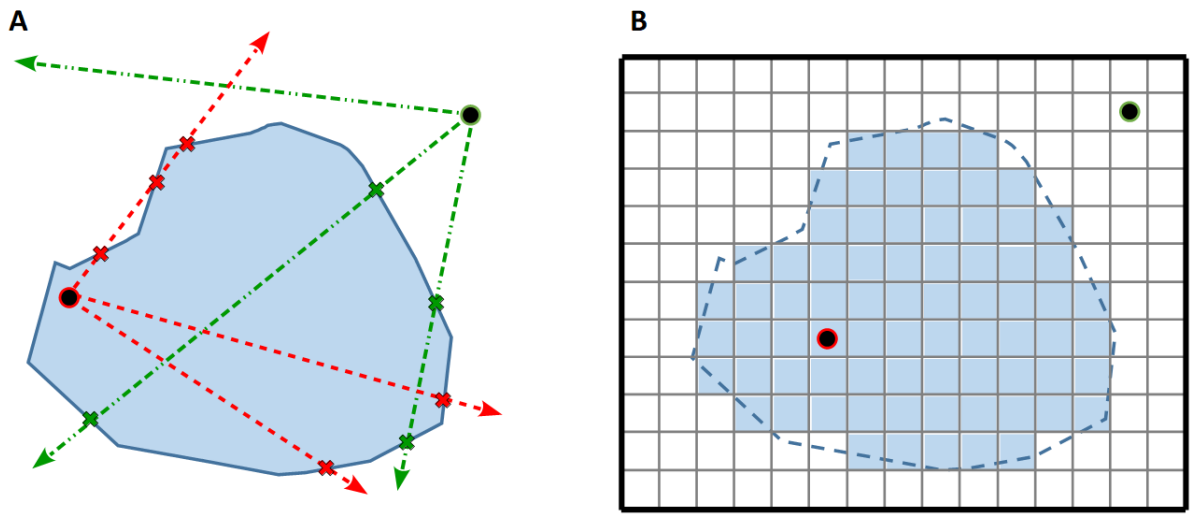


Figure 2: Counting particles in a region of arbitrary shape. A) The surface approach: VOI (blue field) is stored as a triangle mesh (blue line), and the number of intersections ("x" symbols) between rays (dashed lines) and the VOI surface are counted. B) The 3D array approach: VOI is represented as *true* voxels (blue field). VOI boundary is shown as dashed blue line.

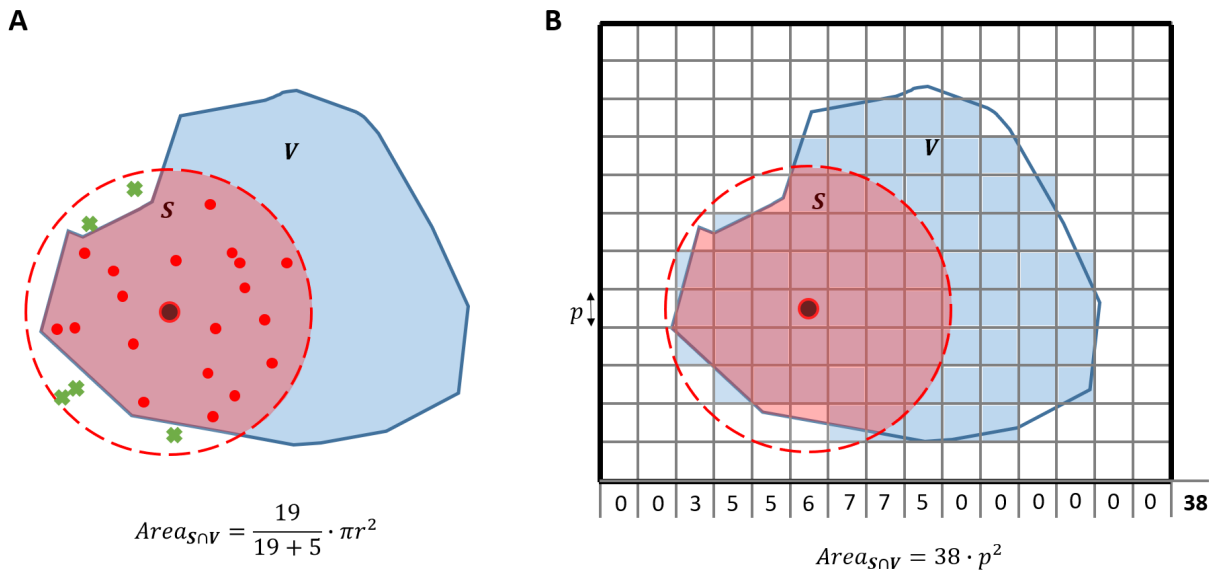


Figure 3: 2D schematics for irregularly bounded area computation. A) MCS algorithm. B) 3D array method.

where V is the ground truth volume (computed analytically) and \hat{V} the estimated volume.

Our data showed that for both spherical and shell edge corrected neighborhoods, 10 - 1000 points and 10 rays per point the MCS algorithm performed well for all neighborhood radii (Fig. S2). As expected, increasing the number of points decreased the variability.

The 3D array algorithm was also very precise, with noticeable errors only for very small neighborhoods, (Fig. S3). This algorithm is expected to be less precise for small and non-flat neighborhoods because in such conditions the discretization of space by voxels deviates from the most the real (curved) shapes.

In comparison, the MCS algorithm required around 1000 particles to reach the precision of the 3D array algorithm. Another advantage of the 3D array algorithm is its non-stochastic nature.

MCS required a larger running time for neighbor size up to 75 voxels and was comparable to 3D array for larger sizes (Fig S4). Here we also used 10 rays per point for MCS. In both algorithms, the running time per volume or area unit decreased with the increased neighborhood size.

2.2.4 Particle overlap

Particles encountered in cryo-ET are not points but have a finite, possibly complex 3D shape. Therefore when a new particle is added to a synthetic null-model instance, it is necessary to ensure that the particle does not overlap with any other particle. Here we use the VTK library to implement volume exclusion between particles. Namely, we first use the VTK library to generate the particle surface at the intended position and orientation specified by Euler angles. Next, we check whether the bounding box of the particle overlaps with any of the other particle bounding boxes. If it does, we use again the iterative ray-firing method implemented in VTK to ensure that no point of a particle surface is inside the surface of any previously inserted particle. If the particles indeed overlap, the new particle is rejected.

2.2.5 Parallel implementation

Second-order metric implementations are very CPU intensive. They require long running times for real data comprising dozens of tomograms and thousands of particles each. Moreover, to achieve a sufficient statistical confidence, more than 100 simulations per tomogram should be computed. To solve both problems, we provide a parallel implementation based on the **multiprocessing** package of the Python programming language, which uses a shared memory environment and exploits the internal parallelism of current multi-core processors.

Specifically, particles are processed separately by n independent *computational units*. To compute the second-order functions for real data, these units are evenly distributed over $p \leq n$ processes that share access to VOI. For each particle, the distance map (Euclidean or geodesic, see Section 3.1.2), is computed once and used for all distances, which minimizes the number of times a distance map has to be computed (Fig. S5A, B). For simulated data, the workload is divided by the number of tomograms to be simulated (m) which are executed by $p \leq m$ processes (Fig. S5C).

The computational speedup [22] obtained by parallelization was almost linear up to 15 processes and continued to increase until the maximum number of processes (35) for both real and simulated data (Fig. S5D). For a high number of processes, the speedup was a little higher for the simulated data. This is beneficial for our applications because most of the workload is generated by the analysis of the null-model. Five synthetic tomograms with 500x500x100 voxels and 200 particles each were used for second-order function computations. To ensure a fair comparison, the number of simulated tomograms on each instance was the same as the number of concurrent processes.

2.2.6 Computational requirements

This software package has been developed in Python and is available open-source (see Code availability), in order to facilitate its dissemination in the research community and the development of future extensions. Graphs are plotted using *matplotlib* library [23], and surface meshes are stored and processed using VTK [21] and visualized through Paraview [24]. All computing experiments were executed on a computer node of the Max Planck Institute of Biochemistry cluster, it has 500GB RAM with 36 processors Intel(R) Xeon(R) CPU E5-2699 v3 @ 2.30GHz with SUSE Linux Enterprise Server 12 SLES 12 SP 1 Operation System.

3 Results

3.1 Validation with synthetic data

3.1.1 Uni- and bivariate functions

To validate the implementation of the second-order metrics, we generated synthetic tomograms that contain randomly distributed and clustered particles (Fig. 4A, B). Particle clusters were generated using Sinusoidal Random Pattern (SRP) distribution \tilde{U} :

$$\tilde{U}((x = q\pi x', y = q\pi y', z = q\pi z') | \sin x + \sin y + \sin z > 3t) \quad (15)$$

where x' , y' and z' are random real numbers uniformly distributed in the interval $[-1, 1]$, $q \in \mathbb{N}$ and $t \in [0, 1]$. Distribution \tilde{U} creates clusters that have oval shape of maximal radius $r_c \approx (q\pi)^{-1} \arccos(3t-2)$ (in x' , y' , z' units). The clusters reach an almost spherical shape for $t > 0.8$, in which case the radius can be approximated by $r_c \approx (q\pi)^{-1} \sqrt{6(1-t)}$. The distance between neighboring clusters (center to center) is $d_{ic} = 2/q$ (in x' , y' , z' units).

Here we generated multiple CSRV, and SRP with volume exclusion (SRPV) synthetic datasets, where SRPV was created from SRP populated with finite size particles (as opposed to point-particles) and excluding overlapping particles. Our software allows using any closed surface to represent particles. For simplicity, here we used spheres with radius $r_p = 5$. This synthetic datasets had a size of $500 \times 500 \times 100$ voxels, where 500 voxels corresponds to x' , y' , and z' interval $[-1, 1]$. For SRPV, we set $q = 4$, and $t = 0.8$, thus generating 16 clusters at the inter-cluster distance of $d_{ic} = 125$ voxels (Fig. 4B).

To validate our implementation of the univariate Ripley's functions, we first checked the L function obtained for the CSRV dataset (the null-model). The mean value of 100 simulations was close to 0 and the $IC5-95\%$ was spread around the 0 value, as expected for a pure random pattern (Fig. 5A, D). This was the case for the whole distance range except for distances lower than $2r_p$, indicating that at short distances particle volume exclusion dominates. We also calculated the L function for additional five CSRV simulations, their mean shows the stochasticity expected for the analysis of real randomly distributed particles.

The univariate Ripley's functions that we obtained for 100 SRPV simulations did not differ between MCS and the 3D array algorithms, Next, we calculated the univariate Ripley's functions L and O functions for the clustered, SRPV, datasets (Fig. 5B, C, E, F). Using the MCS and the 3D array algorithms produced virtually indistinguishable results, as was the case for the CSRV null-model (compare panels A-C and D-F of Fig. 5). The calculated L and O functions for SRPV model showed significant deviations from the results obtained for the CSRV null-model. Specifically, the distance at which function L reached maximum and function O minimum were close to $d_c/2$ and d_c respectively, as expected based on analytical calculations [25]. Furthermore, function L was zero and its first derivative was positive at the distance that corresponds to the inter-cluster distance. This can be explained by observing that the concentration of particles in a neighborhood of radius that equals the periodicity of the point pattern is simply the global particle concentration. At the same distance, function O reached a local maximum, which directly points to clustering at that distance d_{ic} .

Finally, to validate bivariate Ripley's functions, we generated datasets containing two particle sets, the particle sets were spatially uncorrelated in some and spatially correlated with each other in other datasets. The uncorrelated datasets consisted of two independent CSRV patterns (Fig 4C). To generate the correlated datasets, we first generated a CSRV pattern and then placed particles of the second set at distances following the Normal distribution $\mathcal{N}(\mu, \sigma)$ from randomly selected CSRV particles (Figs. 4D and 6.A). For both MCS and the 3D array algorithms, the mean value of the bivariate L function for 100 simulations of the null-model was very close to 0 at all distances, except for the very short ones where the effects of volume exclusion dominate, thus showing that the two sets were independent (Fig. 6B). For the correlated datasets, the bivariate L function of the correlated dataset was significantly different from those obtained for the uncorrelated null-model at an intermediate range of distances. The bivariate L function for the correlated dataset reached significance at the distance of approximately $\mu - \sigma$ and reached a maximum at $\mu + \sigma$, which agrees with the criterion customarily used in the field [25].

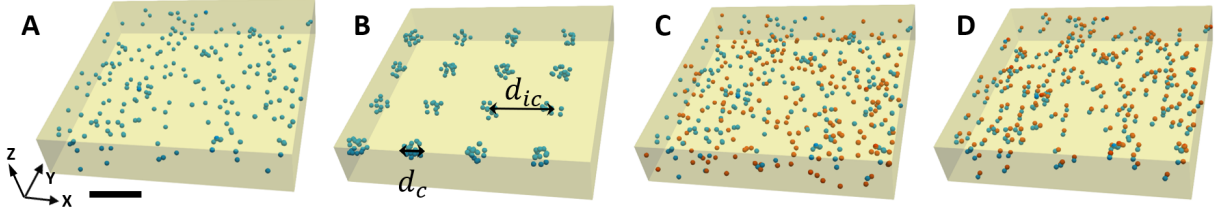


Figure 4: Synthetic datasets used for validations. A) CSRV. B) SRPV with cluster diameter $d_c \approx 46$ voxels and intercluster distance $d_{ic} = 125$. C) Two independently generated CSRV patterns (blue and red). D) CSRV pattern (blue), points of the spatially correlated pattern (red) are located at distances obtained from the normal distribution $\mathcal{N}(\mu = 10, \sigma = 1)$ to the CSRV pattern, we chose the parameters of the normal distribution so that the two patterns visually colocalize. In all cases particles (blue and red) were spheres of radius $r_p = 5$ each particle pattern contained 200 particles and tomograms had size $500 \times 500 \times 100$ voxels. Scale bar 100 voxels.

All together, our implementation of the second-order uni- and bivariate functions on synthetic datasets yielded results that allowed the determination of the correct clustering distance scales. Furthermore, the MCS and the 3D array based implementations produced almost identical results, thus validating both algorithms.

3.1.2 Influence of the distance metric

Because a VOI can have an arbitrary 3D shape and it may include holes, the choice of distance metric d used for defining the neighborhoods \mathcal{S}_L and \mathcal{S}_O , Euclidean or geodesic, can have a strong impact on the computation of the second-order functions. We used the Distance Transform (DT) [26] for computing Euclidean and Fast Marching Method (FMM) algorithm [27] for calculating geodesic distance. We implemented FMM only for the 3D array VOI representation.

For a VOI that has convex shape and trivial topology in 3D (such as that shown on Fig. 6A), Euclidean and geodesic distances are the same, resulting in essentially the same L and O functions (Fig. 6B, C).

However, cellular VOIs often have a complex shape because they are delineated by biological membranes or are formed by a particular distribution of molecular complexes. To evaluate the PPA functions obtained using the two distance metrics, we generated a synthetic dataset where VOI takes the shape of a cropped spherical shell of radius $r_m = 50$ and thickness $t_m = 6$ voxels (Fig. 7A). Such VOIs are encountered for complexes bound to a membrane of a cellular organelle [28]. The particle pattern was formed by four clusters localized in the VOI, and for each cluster i , particles were distributed according to the following expression:

$$\tilde{U}_i(x = x_c + r_m \cos(\phi + \varphi_i) \sin \phi, y = y_c + r_m \sin(\phi + \varphi_i) \sin \phi, z = z_c + r_m \cos \theta) \quad (16)$$

where $c_m = (x_c, y_c, z_c)$ are the coordinates of the VOI, $\mathcal{N}(\mu = 0, \sigma = 0.25)$, r_m is the radius of the VOI θ and ϕ are spherical angles taken from the normal distribution and $\varphi_{1,2,3,4} = \{0, \pi/2, \pi, 3\pi/2\}$ define cluster centers. In this way, the center-to-center inter-cluster distance was $\frac{1}{2}\pi r_m$ (78.5 voxels for r_m of 50 nm) and the cluster size can be approximated by $3\sigma r_m$ (37.5 voxels). In addition, particle distribution $\tilde{U}(x, y, z)$ takes volume exclusion into account.

Our results showed that functions L and O were significantly different from the CSRV null-model. The geodesic distance based L function had the first maximum at approximately 20 voxels ($1.6\sigma r_m$), a 0 crossing with a negative slope at 40 voxels and another with a positive slope at 80 voxels, while the geodesic O function had a local maximum at 80 voxels (Fig. 7B, C). These correspond to the size of the clusters and the distance between them, in the same way that functions L and O did for a simple VOI (Figs 4A and 5B, C, E, F). However, the Euclidean distance based L and O functions showed a shift towards shorter distances. Additionally, the geodesic distance based O function of the null-model particle pattern (CSRV), was almost perfectly flat, as expected for the ideal case (Fig. 7C). The L function for the null-model deviated slightly from the expected 0-value at the largest distances, corresponding to the neighborhoods that reach to the opposite side of the VOI (Fig. 7B). This is likely because the geodesic distance between some of the distant points on

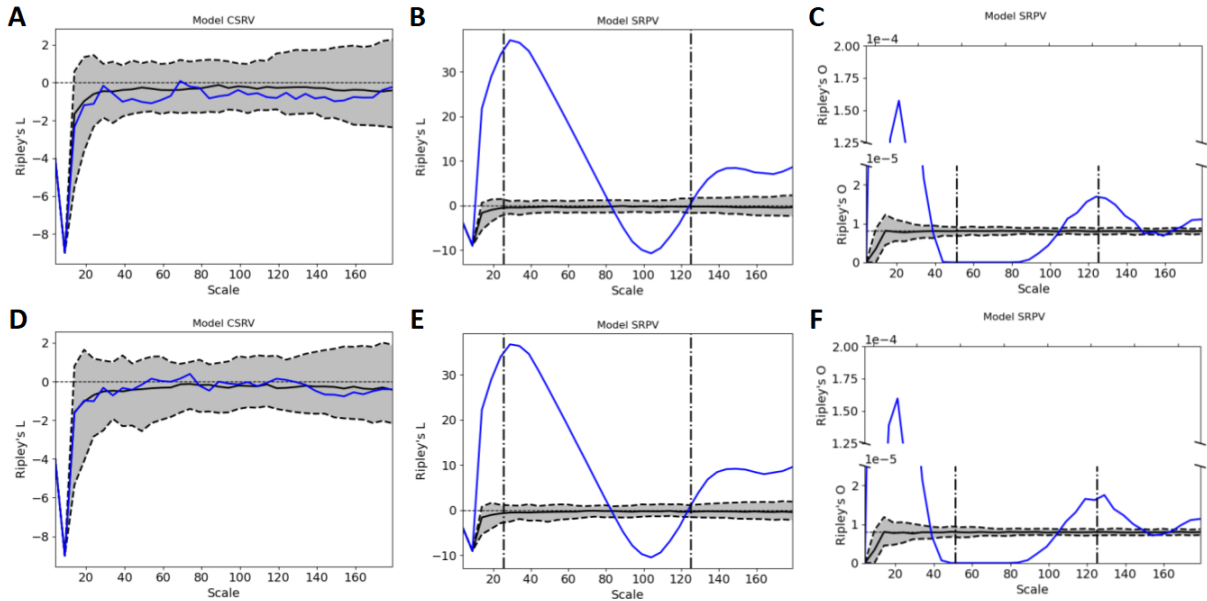


Figure 5: Univariate second-order metrics validation with synthetic datasets. (A-C) 3D array and (D-F) MCS algorithm. (A, D) Function L for CSRV model, blue line shows the mean of additional five CSRV simulations. (B, E) Function L for SRPV model, shown are the mean of five simulations (blue line) and the CSRV null-model (grey). (C, F) Function O for SRPV model, shown are the mean of five simulations (blue line) and the CSRV null-model (grey). In all cases the grey area and line show $IC\ 5 - 95\%$ and the mean of 100 CSRV simulations, respectively. For MCS the number of iterations for convergence is 1000 and the maximum 100000. In (B, E) the vertical dashed lines mark $d_c/2$ and d_{ic} , and in (C, F) d_c and d_{ic} respectively. In (A, B, D, E) the horizontal line marks $X = 0$, and in (C, F) the global density λ , in all cases these lines represent the behavior of the ideal random pattern.

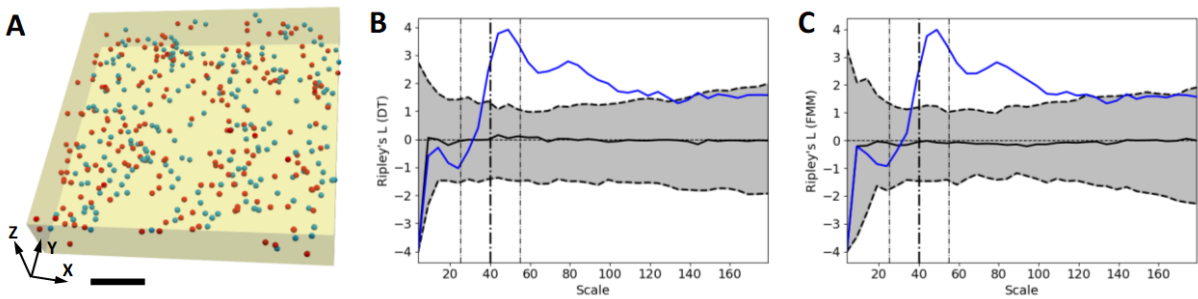


Figure 6: Bivariate second-order analysis validation. (A) Two correlated point patterns where each particle of pattern 2 (red) are placed at a distance controlled by a distribution $\mathcal{N}(\mu = 40, \sigma = 5)$ to a particle of pattern 1 (blue). (B) Function L for the correlated pattern shown in A (mean of 5 simulations) is shown in blue, and the $IC\ 5 - 95\%$ of 100 simulated uncorrelated pairs in gray. Distances were measured using Distance Transform (DT). (C) Like B except that Fast Marching Method (FMM) was used for distance computation. (B, C) Thick vertical lines represent $r = \mu$ and the thin ones $r = \mu \pm 3\sigma$. Tomograms size $500 \times 500 \times 100$. Scale bar 100 voxels.

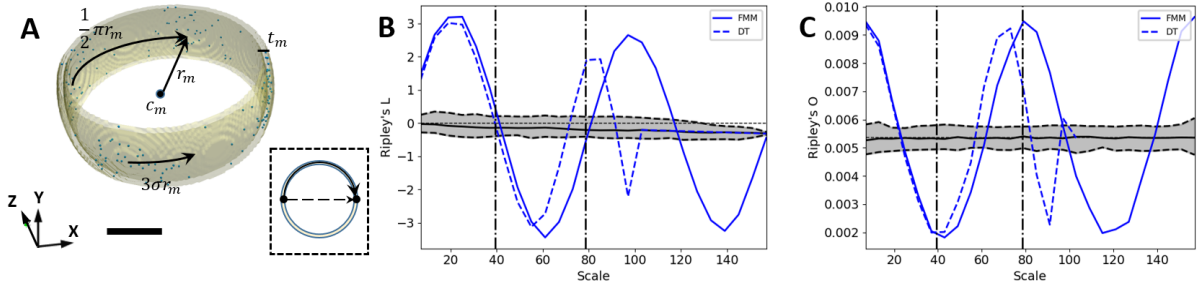


Figure 7: Geodesic and Euclidean distance based second order functions on a complex VOI. (A) A biological membrane-like VOI, $r_m = 50$, and $\sigma = 0.25$ containing clustered particles (blue points). The inset shows the difference between geodesic (solid arrow) and Euclidean distances (dashed arrow) between two points on the opposite sides of a sphere. (B) Function L and (C) function O for the clustered particle pattern (blue lines) and the null-model ($IC\ 5 - 95\%$ in gray, black line represents the mean). In both cases the second order functions based on geodesic distance (solid and blue line) and Euclidean distance (dashed blue line) are shown. Scale bar 30 voxels.

the cropped spherical shell VOI differs from the geodesic distance on a full spherical shell. Therefore, our results show that using FMM allows an accurate determination of the geodesic distance and that for membrane-like compartments and other complex shape VOIs, the PPA functions should be calculated based on geodesic and not Euclidean distances for .

3.2 Experimental data

We proceeded to validate the computational methods described in previous sections on experimental data. To this end, we applied the first and second order PPA functions to study the organization of ribosomes in yeast cells visualized by cryo-ET. We used data from two experimental groups, each comprising a set of tomograms from yeast cell cytoplasm imaged *in situ*. The first set contains 13 tomograms of yeast cells that were treated with Rapamycin and the second 14 tomograms of untreated cells [29]. In both cases, cell cytoplasm was segmented, ribosomes were localized by template matching and a high resolution structure of ribosomes (obtained from EMD-3068) was used to represent the ribosome shape, as shown on a slice of a labeled tomogram (Fig. 8A).

We calculated the first-order functions for each tomogram separately in order to determine the lengths that characterize the organization of ribosomes (Fig. 8.B-E). In untreated cells, the nearest neighbor function showed a clear peak that represents the most common nearest-ribosome distance. For each tomogram, multiple null-model distributions were generated, each having the same VOI and the same number of ribosomes as the corresponding tomogram. All functions (G , F , and J) showed that ribosomes are significantly clustered with respect to the null-model (CSR_V). This is in agreement with the expected aggregation of functional ribosomes to form poly-ribosomes. More generally, this type of analysis can help describing macromolecular interactions [2, 17]. However, it is not straightforward to combine the first order functions of individual tomograms within an experimental group to obtain a single function that characterizes an experimental condition, because the particle concentration within VOIs differ between the cells even though they were grown under identical conditions, which influences the first order functions (Fig. 8F-I).

Second-order PPA functions were calculated for each tomogram separately, as well as for their respective CSR_V null-models (Fig. 9). The null-model L functions for different tomograms and different experimental groups (control and Rapamycin treated) were very similar. The experimental group means were almost indistinguishable, only the variability was higher for the Rapamycin set likely because of the lower number of particles (Fig. 9.A). In contrast, function O for the null-model was very different for different tomograms and there was a clear separation between the two experimental groups. Because this variability was likely due to the different global particle concentration in the tomograms, we here propose to use the radial distribution function $g(r)$ [30], which is computed by normalizing function O by the global particle concentration:

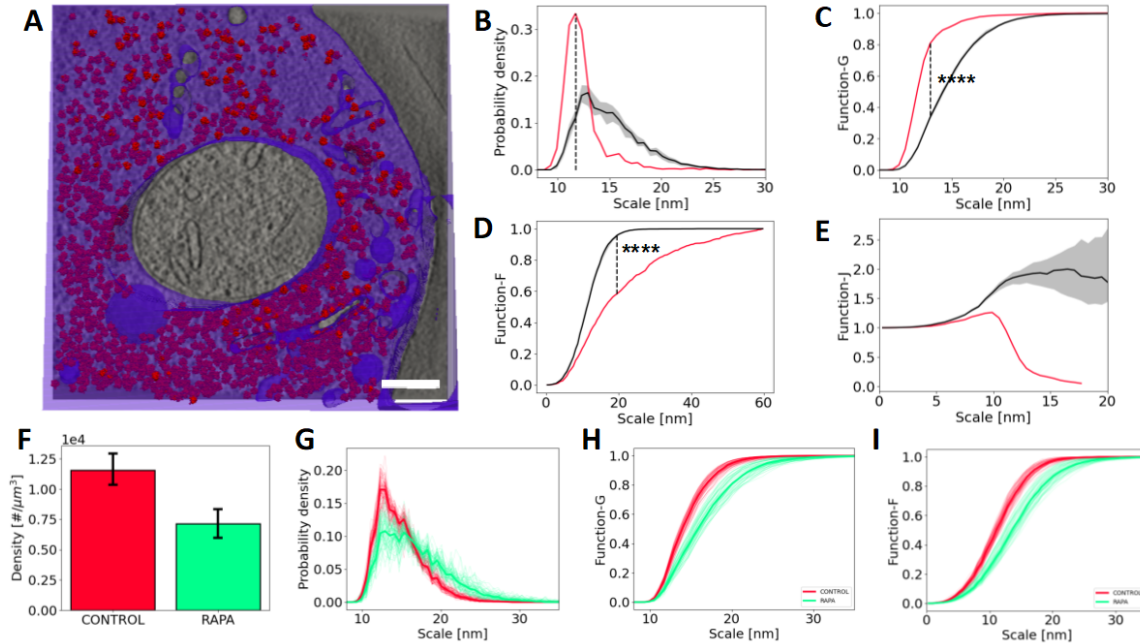


Figure 8: First-order analysis of experimental data. A) Tomographic slice of the analyzed cryo-tomograms, with overlay showing segmented cytoplasm (VOI, transparent blue) and localized ribosomes (red), scale bar 200 nm. B) Histogram of all nearest neighbor distances (function G), dashed vertical line marks the most frequent nearest neighbor distance. C) Function G shown as a cumulative distribution (K-S test, $D_{2182,20} = 0.4703$ and $\alpha < 0.0001$). D) Spatial contact distribution function (F) with 1000 simulated points (K-S test, $D_{1000,20} = -0.3743$ and $\alpha < 0.0001$). E) Function J . B-E) The functions obtained from the experimental data are shown in red. CSRV null-model simulation means are shown in black and IC 5 – 95% in grey (20 simulations for each tomogram). Dashed vertical lines show $D_{n,m}$. F-I) Comparison between the two sets of tomograms, control (CONTROL, red), and Rapamycin treated (RAPA, green). F) Particle density within the VOIs, mean and IC 5 – 95%. G) Function G shown as histogram. H) Function G shown as the cumulative distribution. I) Function F . G-I) Analyses of individual simulated null-models are shown as thin lines, thick lines show the means. In all cases Euclidean distance was used.

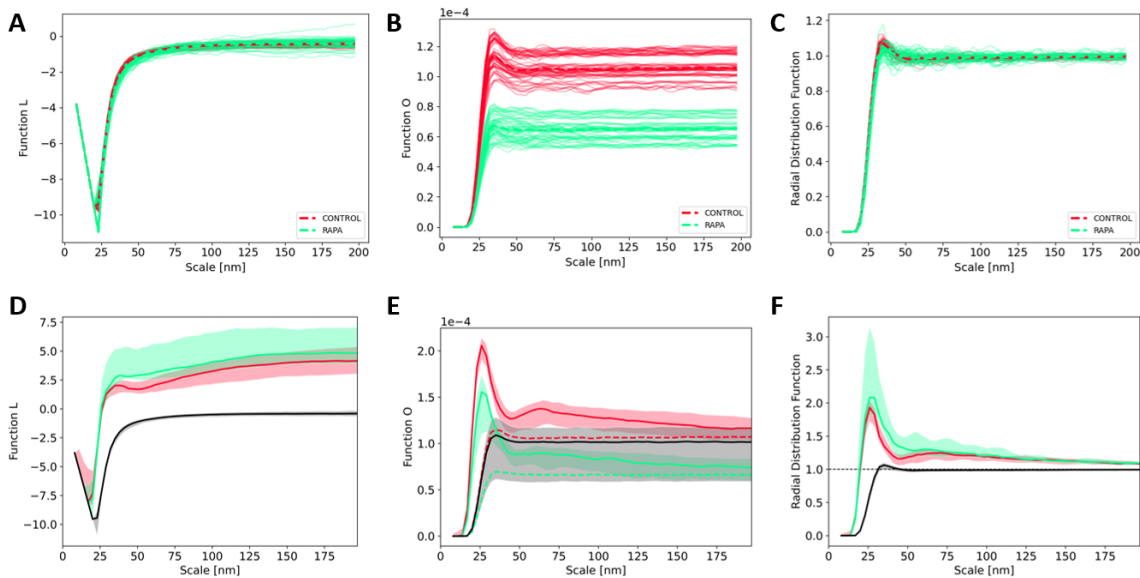


Figure 9: Second-order analysis for experimental and the corresponding CSRV null-model data. A-C) Functions obtained for CSRV null-model data corresponding to the control (CONTROL, red) and Rapamycin treated (RAPA, green) tomograms. Each thin semi-transparent line represents a CSRV null-model simulation, five per tomogram, the thick dashed lines show the means. D-F) Functions obtained for experimental tomograms, control (CONTROL, red) and Rapamycin treated (RAPA, green). Pooled null-model simulations (untreated and Rapamycin treated) IC 5 – 95% is shown in grey and the mean in black. E) Also shows the mean simulations of the experimental groups (dashed lines). A, D) Function L . B, E) Function O . C, F) Radial distribution function.

$$g(r) = \frac{1}{\lambda} O(r) \quad (17)$$

This normalization restored the low variability of the null-model simulations between tomograms and experimental groups (see Fig. 9.C).

When applied to the experimental data, the L and the radial distribution functions clearly showed significant clustering, both for all tomograms taken together and for the experimental groups taken separately (Fig. 9.D, F). In both experimental cases the first maximum was located around 25 nm, which approximately corresponds to the double of the most frequent nearest neighbor distance (8.B). While the large variability between the groups obtained for the function O precludes the interpretation of all tomograms taken together, each of the experimental group showed significant clustering when compared to the corresponding null-model (Fig. 9B, E). While it is expected that in the untreated cells the formation of polyribosomes leads to ribosome clustering, our results show that some form of ribosome clustering persists in the Rapamycin treated cells.

Furthermore, in order to set the stage for a statistical comparison between the experimental groups, we computed the mean and IC 5 – 95% as we did before, except that because of the low number of tomograms, the IC contains all tomograms. This comparison is valid for L and radial distribution function as null-models converge to a similar IC . However, in our case, this approach can not be applied to function O , because we already saw that it is sensitive to particle global densities and the two experimental groups contain different number of particles. The statistical significance between the groups can be easily established for distances at which the L and the radial distribution functions show clear separation between the experimental groups. To determine the significance at other distances, non-parametric inference tests could be applied to values of the second order functions.

4 Discussion

Here we implemented the first and second-order, mono- and bivariate PPA functions for 3D VOIs of arbitrary shape. This is of particular importance for the analysis of molecular complexes visualized in 3D biological images, such as those obtained by cryo-ET of cellular samples, because cellular regions often have complex, non-convex shape. These cellular regions can be formed by lipid membrane-bounded organelles and vesicles, membranes where certain membrane-bound complexes reside, or any other cellular regions that constrain the localization of molecular complexes of interest. Furthermore, because molecular complexes occupy a substantial part of the cellular volume and the influence of their size cannot be neglected at short distances, we represented molecular complexes as 3D objects and imposed volume exclusion to prevent the overlap.

The implementation of the second-order functions was particularly important because they are sensitive to clustering at multiple distance scales, thus providing more information than the first order functions. It critically depends on solving two tasks; (1) determination of the number of particles located within an irregularly bounded spatial region and (2) measuring the volume of this space. The solutions depend on the approach taken to represent spatial regions (particle neighborhoods and VOI). In the first approach, we represented spatial regions by a triangular surface mesh that defines the region boundary. Here we used the stochastic ray-firing algorithm to count the number of particles and MCS for the volume determination. The second approach we implemented is based on representing spatial regions as 3D binary arrays, which makes the implementation of the two tasks trivial. In theory, ray-firing and MCS are stochastic methods that can achieve any precision and are independent of the volume shape. 3D array based methods are deterministic and they typically use more memory than the surface based methods. However, our results show that for the same computational time, the 3D array-based methods achieved a higher precision than the surface-based counterparts. Nevertheless, the second order PPA functions that we computed using these two approaches were virtually indistinguishable.

We validated the implementation of the second-order, uni- and bi-variate PPA functions on synthetic datasets. Our software correctly detected the clustering distance scales that characterized the particle distribution in the synthetic datasets. Additionally, we implemented the PPA functions based on both Euclidean and geodesic distances, verified that they produced the correct results, and showed that for simple VOIs the Euclidean and the geodesic results were the same. Importantly, the geodesic distance based second order PPA functions were more suitable for applications involving complex VOIs, such as for describing the nanodomain organization of molecular complexes located on curved membranes, the situation commonly encountered in cellular environments.

Because analytical solutions for the PPA functions do not exist for complex VOI and particle geometries, synthetic random tomograms (null-models) are required in order to determine the statistical significance of the PPA functions applied to experimental data. The inherent variability of cellular components and the fact that a typical cellular cryo-ET dataset contains tens of tomograms necessitate generating a set of synthetic random model tomograms for each experimental tomograms. An experimental tomogram and its corresponding synthetic tomograms have to have the same VOI and the number of particles. Furthermore, a large number of synthetic tomograms is needed to allow reaching a specified significance level. To alleviate the computational burden involved in the generation of the necessary number of random models and the computationally intensive calculation of the PPA functions for all tomograms, we propose a multi-process implementation of these routines that reduced the running times, thus enabling the effective analysis of realistic datasets. We achieved a speed-up factor of approximately 15 using a single processor multi-core architecture, a similar value to those recently obtained in [31] where a cluster of computers was used for computing space-time Ripley's K .

Application of our software to yeast cell cytoplasm imaged by cryo-ET allowed us to detect ribosome clustering and determine the characteristic distance scales. Furthermore, we showed that the second order functions, in particular L and the radial distribution functions, were better suited to compare experimental groups comprising multiple tomograms because they were not sensitive to the global concentration of particles.

Future applications of our software are also expected to provide a spatial characterization of macromolecular crowding, as well as liquid and lipid phase separation. These processes recently gained a significant biological interest, because they were shown to affect biochemical reactions in cells and global organization of cellular membranes and regions in different cellular systems [32, 33].

Therefore, our implementation of the PPA functions provides a tool that can characterize simultaneous

clustering at multiple distance scales, which is suitable for applications to cellular molecular complexes visualized by cryo-ET, as well as to other 3D systems where real-size particles are located within regions possessing complex geometry.

Acknowledgments

We thank S. Pfeffer and B. Engel for giving us access to their cryo-ET experimental data. This work was supported by the European Commission (grant no. FP7 GA ERC-2012-SyG_318987– ToPAG) the Deutsche Forschungsgemeinschaft (DFG, German Research Foundation) under Germany's Excellence Strategy - EXC 2067/1- 390729940 and by Max Planck Society. We would like to thank Gabriela J. Greif for critical reading of the manuscript.

Code availability

PyOrg code belongs to a more general public repository (pyseg_system, https://github.com/anmartinezs/pyseg_system) which contains additional software, tests, and dependencies. The code of PyOrg alone and can be downloaded from https://github.com/anmartinezs/pyseg_system/tree/master/pyseg-sys/pyorg.

References

- [1] Diana M Mitrea and Richard W Kriwacki. Phase separation in biology; functional organization of a higher order. *Cell Communication and Signaling*, 14(1):1–20, 2016.
- [2] Elizabeth S Freeman Rosenzweig, Bin Xu, Luis Kuhn Cuellar, Antonio Martinez-Sanchez, Miroslava Schaffer, Mike Strauss, Heather N Cartwright, Pierre Ronceray, Jürgen M Plitzko, Friedrich Förster, et al. The eukaryotic co-2-concentrating organelle is liquid-like and exhibits dynamic reorganization. *Cell*, 171(1):148–162, 2017.
- [3] Vlado Lučić, Alexander Rigort, and Wolfgang Baumeister. Cryo-electron tomography: The challenge of doing structural biology in situ. *The Journal of cell biology*, 202(3):407–419, 2013.
- [4] K. A. Taylor and R. M. Glaeser. Electron diffraction of frozen, hydrated protein crystals. *Science*, 186(4168):1036–7, Dec 13 1974.
- [5] Jacques Dubochet, Marc Adrian, Jiin-Ju Chang, Jean-Claude Homo, Jean Lepault, Alasdair W McDowell, and Patrick Schultz. Cryo-electron microscopy of vitrified specimens. *Quarterly reviews of biophysics*, 21(2):129–228, 1988.
- [6] T. Wiegand and K. A. Moloney. Rings, circles, and null-models for point pattern analysis in ecology. *Oikos*, 104(2):209–229, 2004.
- [7] Eric Marcon and Florence Puech. Evaluating the geographic concentration of industries using distance-based methods. *Journal of Economic Geography*, 3(4):409–428, 2003.
- [8] Gilles Duranton and Henry G Overman. Testing for localization using micro-geographic data. *The Review of Economic Studies*, 72(4):1077–1106, 2005.
- [9] Sarah J Plowman, Cornelia Muncke, Robert G Parton, and John F Hancock. H-ras, k-ras, and inner plasma membrane raft proteins operate in nanoclusters with differential dependence on the actin cytoskeleton. *Proceedings of the National Academy of Sciences*, 102(43):15500–15505, 2005.

- [10] Dylan M Owen, Carles Rentero, Jérémie Rossy, Astrid Magenau, David Williamson, Macarena Rodriguez, and Katharina Gaus. Palm imaging and cluster analysis of protein heterogeneity at the cell surface. *Journal of biophotonics*, 3(7):446–454, 2010.
- [11] P. Andrey, K. Kieu, C. Kress, G. Lehmann, L. Tirichine, Z. Liu, E. Biot, P. G. Adenot, C. Hue-Beauvais, N. Houba-Herlin, V. Duranthon, E. Devinoy, N. Beaujean, V. Gaudin, Y. Maurin, and P. Debey. Statistical analysis of 3D images detects regular spatial distributions of centromeres and chromocenters in animal and plant nuclei. *PLoS Computational Biology*, 6(7):e1000853, 2010.
- [12] Mehrdad Jafari Mamaghani, Mikael Andersson, and Patrik Krieger. Spatial point pattern analysis of neurons using ripley’s k-function in 3d. *Frontiers in neuroinformatics*, 4:9, 2010.
- [13] WSD Wong and Jay Lee. *Statistical analysis of geographic information with ArcView GIS and ArcGIS*. Wiley, 2005.
- [14] Kristin Hansson, Mehrdad Jafari-Mamaghani, and Patrik Krieger. Ripleygui: software for analyzing spatial patterns in 3d cell distributions. *Frontiers in neuroinformatics*, 7:5, 2013.
- [15] François Goreaud and Raphaël Pélissier. On explicit formulas of edge effect correction for ripley’s k-function. *Journal of Vegetation Science*, 10(3):433–438, 1999.
- [16] Leonid Andronov, Jonathan Michalon, Khalid Ouararhni, Igor Orlov, Ali Hamiche, Jean-Luc Vonesch, and Bruno P Klalholz. 3dclustervis: 3d clustering analysis of super-resolution microscopy data by 3d voronoi tessellations. *Bioinformatics*, 34(17):3004–3012, 2018.
- [17] Marion Jasnin, Florian Beck, Mary Ecke, Yoshiyuki Fukuda, Antonio Martinez-Sanchez, Wolfgang Baumeister, and Günther Gerisch. The architecture of traveling actin waves revealed by cryo-electron tomography. *Structure*, 27(8):1187–1189, 2019.
- [18] Antonio Martinez-Sanchez, Ulrike Laugks, Zdravko Kochovski, Christos Papantoniou, Luca Zinzula, Wolfgang Baumeister, and Vladan Lučić. Trans-synaptic assemblies link synaptic vesicles and neuroreceptors. *Science Advances*, 7(10):eabe6204, 2021.
- [19] Jose-Jesus Fernandez. Computational methods for electron tomography. *Micron*, 43(10):1010–1030, 2012.
- [20] J. L. Hodges. The significance probability of the smirnov two-sample test. *Arkiv för Matematik*, 3(5):469 – 486, 1958.
- [21] Will Schroeder, Ken Martin, and Bill Loresen. *The Visualization Toolkit (4th ed.)*. Kitware, 2006.
- [22] Gene M Amdahl. Validity of the single processor approach to achieving large scale computing capabilities. In *Proceedings of the April 18-20, 1967, spring joint computer conference*, pages 483–485, 1967.
- [23] J. D. Hunter. Matplotlib: A 2d graphics environment. *Computing In Science & Engineering*, 9(3):90–95, 2007.
- [24] Utkarsh Ayachit. The paraview guide: a parallel visualization application. 2015.
- [25] M. A. Kiskowski, J. F. Hancock, and A. K. Kenworthy. On the use of Ripley’s K-function and its derivatives to analyze domain size. *Biophysical Journal*, 97(4):1095–1103, 2009.
- [26] Ingemar Ragnemalm. The euclidean distance transform in arbitrary dimensions. *Pattern Recognition Letters*, 14(11):883–888, 1993.
- [27] James A Sethian. A fast marching level set method for monotonically advancing fronts. *Proceedings of the National Academy of Sciences*, 93(4):1591–1595, 1996.

- [28] A. Martinez-Sanchez, Zdravko Kočovski, Ulrike Laugks, Johannes Meyer zum Alten Borgloh, Stefan Pfeffer, Wolfgang Baumeister, and Vladan Lucic. Template-free detection and classification of membrane-bound complexes in cryo-electron tomograms. *Nature Methods*, 17(2):209–216, 2020.
- [29] Morgan Delarue, Gregory P Brittingham, Stefan Pfeffer, IV Surovtsev, S Pingley, KJ Kennedy, M Schaffer, JI Gutierrez, D Sang, G Poterewicz, et al. mtorc1 controls phase separation and the biophysical properties of the cytoplasm by tuning crowding. *Cell*, 174(2):338–349, 2018.
- [30] David Chandler. Introduction to modern statistical. *Mechanics. Oxford University Press, Oxford, UK*, 40, 1987.
- [31] Yuan Wang, Zhipeng Gui, Huayi Wu, Dehua Peng, Jinghang Wu, and Zousen Cui. Optimizing and accelerating space-time ripley’s k function based on apache spark for distributed spatiotemporal point pattern analysis. *Future Generation Computer Systems*, 2019.
- [32] Maryna Löwe, Milara Kalacheva, Arnold J. Boersma, and Alexej Kedrov. The more the merrier: effects of macromolecular crowding on the structure and dynamics of biological membranes. *The FEBS Journal*, 287(23):5039–5067, 2020.
- [33] Xudong Chen, Xiandeng Wu, Haowei Wu, and Mingjie Zhang. Phase separation at the synapse. *Nature Neuroscience*, 23(3):301–310, feb 2020.
- [34] George EP Box, Mervin E Muller, et al. A note on the generation of random normal deviates. *The annals of mathematical statistics*, 29(2):610–611, 1958.

Supplementary material

Algorithm S1 Computation of the volume of one particle edge corrected neighborhood by MCS method.

Require: c : Particle center, r : Scale, \mathcal{V} : cellular compartment, N : Num. iterations to converge, M : Max. number of iterations

Ensure: $\hat{V}(\mathcal{S}(c, r))$: Volume for a particle neighborhood embedded in \mathcal{V}

$N_{hits} \leftarrow 0, N_{iter} \leftarrow 0$

while $(N_{hits} \leq N) \wedge (N_{iter} \leq M)$ **do**

$N_{iter} \leftarrow N_{iter} + 1$

$\mathbf{x} \leftarrow c + \text{gen_rand_coordinate}(r)$ \triangleright For function L use the 3-ball algorithm, for function O the 2-sphere

if $\mathbf{x} \in \mathcal{V}$ **then**

$N_{hits} \leftarrow N_{hits} + 1$

end if

end while

$\hat{V}(\mathcal{S}) = (N_{hits}/N_{iter}) \cdot V(\mathcal{S}(c))$

Algorithm S2 Uniformly sampling the 2-sphere, adapted from the Müller-Box algorithm [34].

Require: r : Neighbourhood scale

Ensure: \mathbf{s} : Random sample in the 2-sphere

$\mathbf{x} \leftarrow (\mathcal{N}(0, 1), \mathcal{N}(0, 1), \mathcal{N}(0, 1))$ $\triangleright \mathcal{N}(\mu, \sigma)$: is the normal random distribution with parameters μ and σ

$\mathbf{s} = r \cdot \frac{\mathbf{x}}{\|\mathbf{x}\|}$

Algorithm S3 Uniformly sampling the 3-ball, adapted from the Müller-Box algorithm [34].

Require: r : Neighbourhood scale

Ensure: \mathbf{s} : Random sample in the 3-ball

$\mathbf{x} \leftarrow (\mathcal{N}(0, 1), \mathcal{N}(0, 1), \mathcal{N}(0, 1))$

$\triangleright \mathcal{U}$: is the uniform random distribution in $[0, 1]$

$\mathbf{s} = r \cdot \mathcal{U}^{1/3} \cdot \frac{\mathbf{x}}{\|\mathbf{x}\|}$

Algorithm S4 3D array volume computation algorithm.

Require: c : Particle center, $\{r_1, \dots, r_n\}$: set of n scales, \mathcal{V} : (optional) Shell thickness t

Ensure: $\hat{V}_1(\mathcal{S}(c, r_1)), \dots, \hat{V}_n(\mathcal{S}(c, r_n))$: Volumes for all particle neighborhoods embedded in \mathcal{V}

$\mathcal{V}^{r_{\max}} = \{x \in \{\mathcal{V} \wedge \mathcal{S}(c, r_{\max})\}\}$

$\mathcal{D} \leftarrow \text{distance_transform}(\mathcal{V}^{r_{\max}})$

for all $r_i \in r_1, \dots, r_n$ **do**

$S \leftarrow \text{gen_binary_mask}(c, r_i, \mathcal{D})$

$\hat{V}_i(\mathcal{S}(c, r_i)) = \sum S$

end for

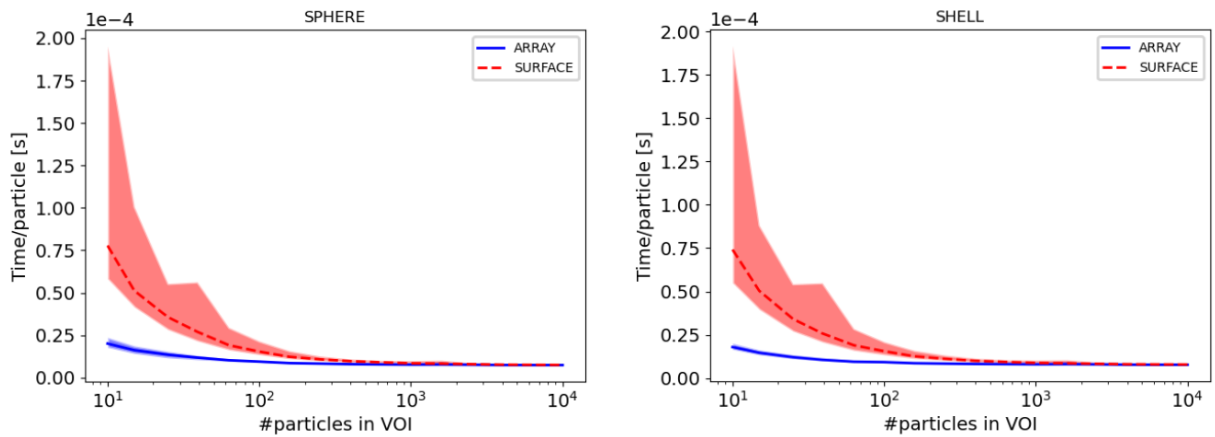


Figure S1: Running time for evaluating the condition $x \in \mathcal{V}$ (whether a particle belongs to VOI). Two different VOIs were used, a sphere (left) and a thin spherical shell (right). The running times per particle are shown for the surface and the 3D array representations of VOI. The line center represents the median of 100 simulations and thickness the interval of confidence [5, 95] %.

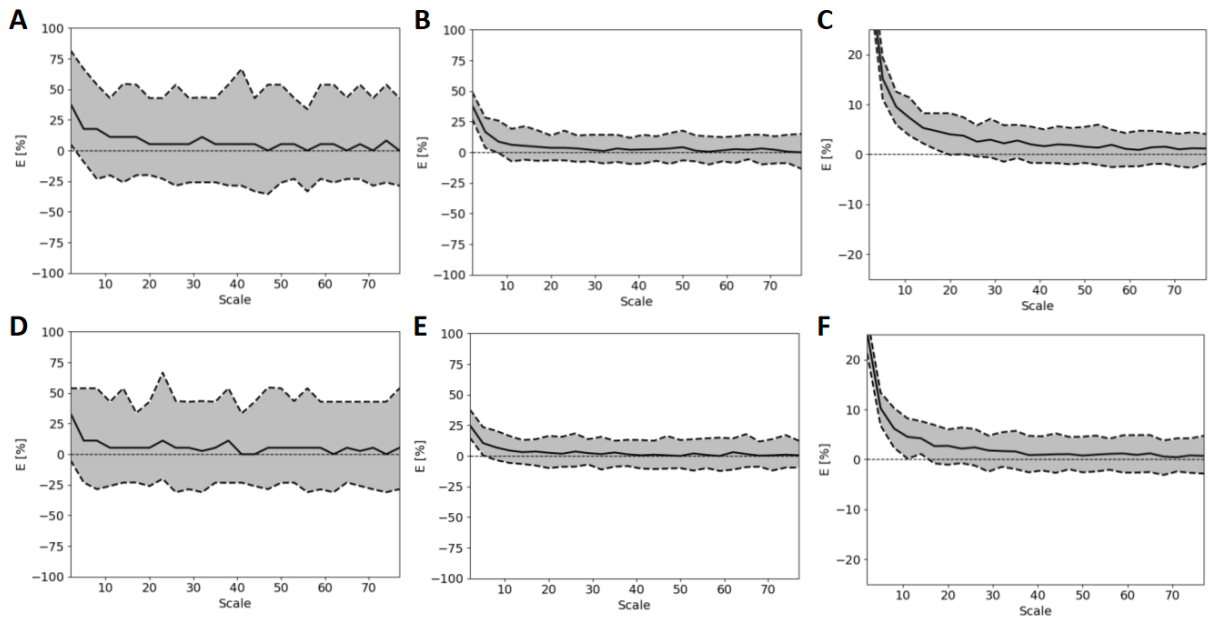


Figure S2: Volume estimate precision for MCS algorithm. (A-C) Half-spherical neighborhoods and (D-F) shell neighborhood, (A,D) $N = 10$, (B,E) $N = 100$ and (C,F) $N = 1000$, where N is the number of points. Solid lines are the median of 1000 executions and $IC = [5, 95]\%$ in gray. $N_{rays} = 10$.

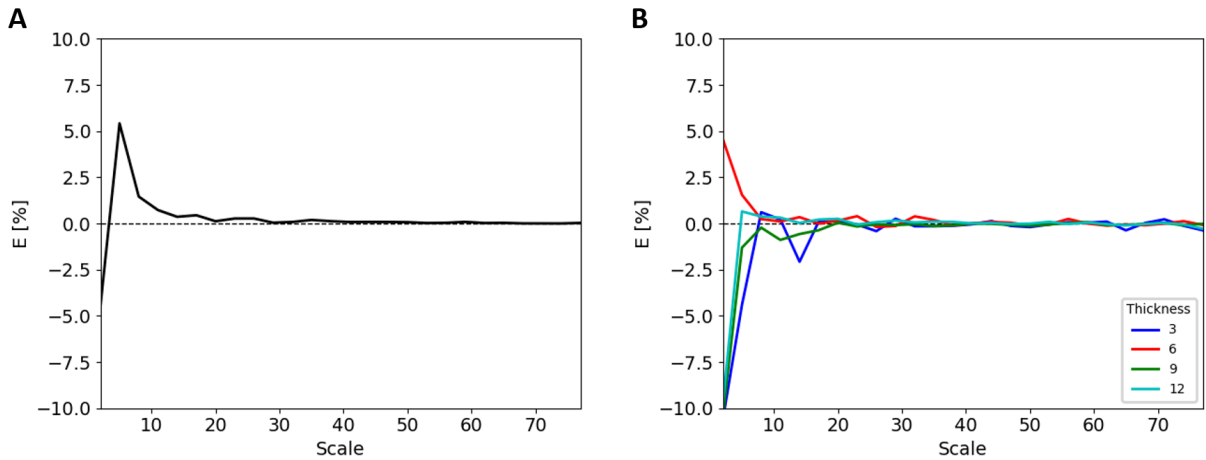


Figure S3: Volume estimate precision for the 3D array algorithm. A) Half-spherical neighborhoods B) Shell neighborhoods, the shell thickness is indicated on the graph.

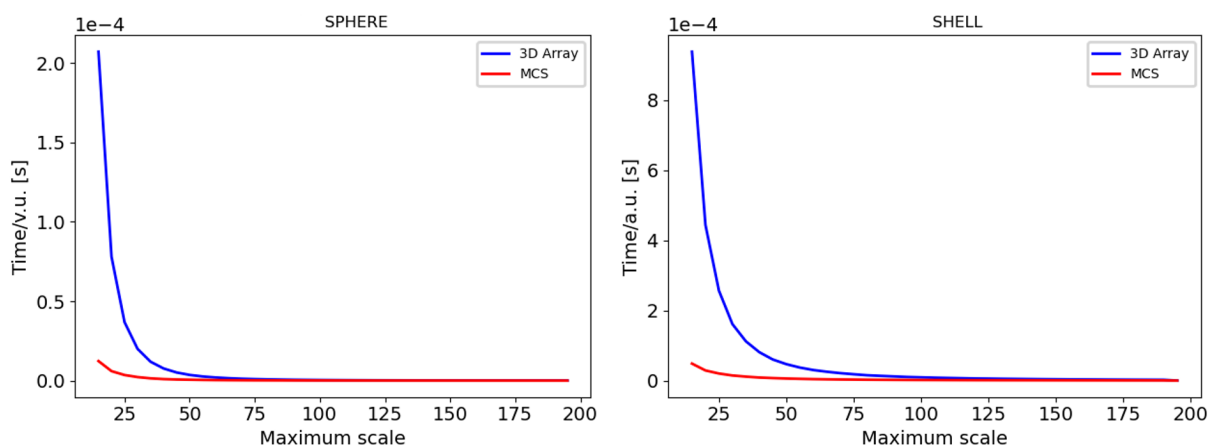


Figure S4: Execution time comparison for volume determination with MCS and 3D array algorithms. A) Running time per volume unit for spherical neighborhoods B) Running time per area unit for shell neighborhoods. In both cases points were randomly distributed. The neighborhoods had different sizes, ranging from 15 to the maximum size as indicated on X-axes.

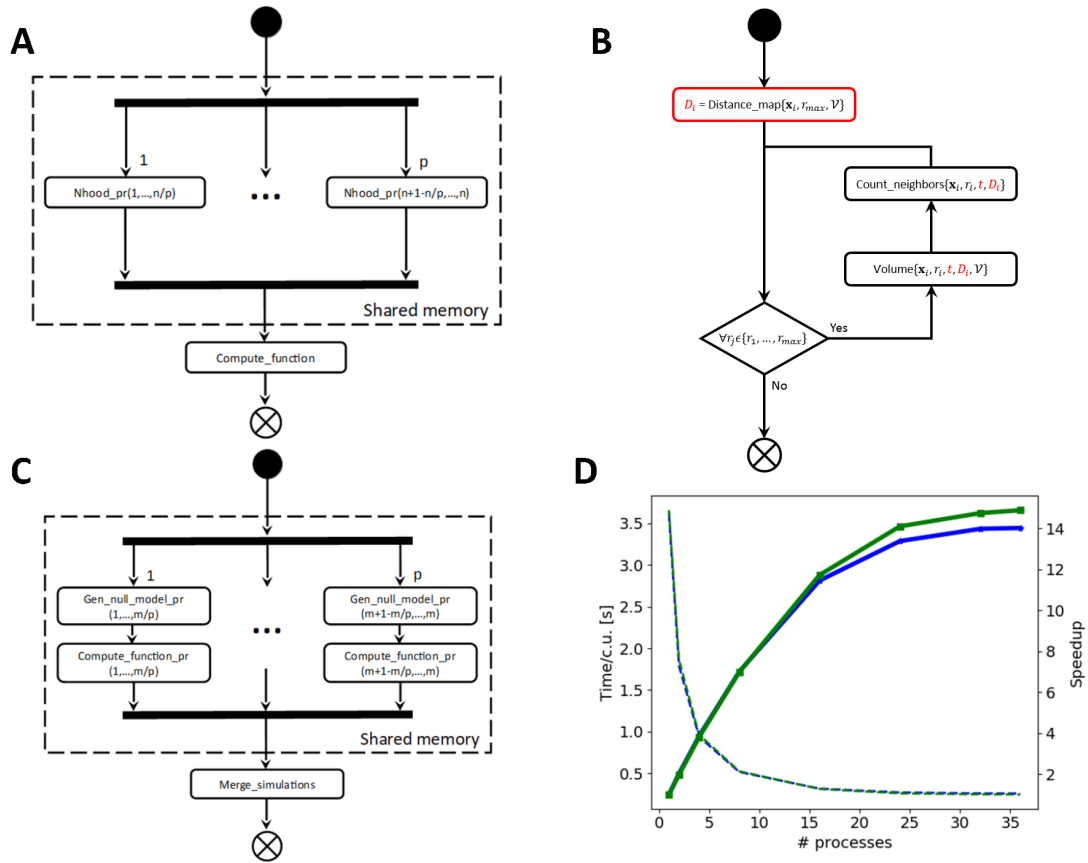


Figure S5: Parallelization diagrams and execution speedup for the second-order functions computations. A) Activity diagram for processing real data using, $p \leq n$ concurrent processes (n is the number of particles). B) Diagram of tasks within a single processing unit (**Nhood_pr**) including the calculations of the number of neighbors and the neighborhood volumes for a range of distances $\{r_1, \dots, r_{max}\}$ (computing unit, c.u.). Operations and parameters shown in red are only required for the 3D array but not for MCS algorithm. C) Activity diagram for processing simulated data using $p \leq m$ processes concurrently (m is the total number of simulated tomograms). D) Execution time per c.u. (dashed lines) and the speedup (solid lines) obtained with different amounts of concurrent processes. Computations for experimental data (blue), and simulations (green). Five synthetic tomograms with $500 \times 500 \times 100$ pixels and 200 particles each were used for experimental data computation. To ensure a fair comparison, the number of simulated tomograms on each instance was the same as the number of concurrent processes.